



# Optical Coherence Tomography Enabling Non Destructive Metrology of Layered Polymeric GRIN Material

Panomsak Meemon<sup>1,5</sup>, Jianing Yao<sup>1</sup>, Kye-Sung Lee<sup>1</sup>, Kevin P. Thompson<sup>1,2</sup>, Michael Ponting<sup>3,4</sup>, Eric Baer<sup>4</sup> & Jannick P. Rolland<sup>1</sup>

<sup>1</sup>The Institute of Optics, University of Rochester, Rochester, NY 14627, <sup>2</sup>Synopsys Inc., 3 Graywood Ln, Pittsford, NY 14534, <sup>3</sup>PolymerPlus LLC, Valley View, OH 44125, <sup>4</sup>Case Western Reserve University, Cleveland, OH 44106, <sup>5</sup>School of Laser Technology and Photonics, Institute of Science, Suranaree University of Technology, Nakhon Ratchasima, Thailand 30000.

SUBJECT AREAS:  
POLYMERS  
COMPOSITES  
CHARACTERIZATION AND  
ANALYTICAL  
TECHNIQUES  
IMAGING TECHNIQUES

Received  
27 December 2012

Accepted  
8 April 2013

Published  
23 April 2013

Correspondence and  
requests for materials  
should be addressed to  
J.P.R. (rolland@optics.  
rochester.edu)

Gradient Refractive INDEX (GRIN) optical components have historically fallen short of theoretical expectations. A recent breakthrough is the manufacturing of nanolayered spherical GRIN (S-GRIN) polymer optical elements, where the construction method yields refractive index gradients that exceed 0.08. Here we report on the application of optical coherence tomography (OCT), including micron-class axial and lateral resolution advances, as effective, innovative methods for performing nondestructive diagnostic metrology on S-GRIN. We show that OCT can be used to visualize and quantify characteristics of the material throughout the manufacturing process. Specifically, internal film structure may be revealed and data are processed to extract sub-surface profiles of each internal film of the material to quantify 3D film thickness and homogeneity. The technique provides direct feedback into the fabrication process directed at optimizing the quality of the nanolayered S-GRIN polymer optical components.

In optical systems, the ability to produce a Spherical Gradient in Refractive INDEX (S-GRIN) has important and far-reaching implications. In nature, many species have eyes with S-GRIN lenses that empower them with greater focusing power, sharper images, and a lower number of components<sup>1–4</sup>. Fish eyes can have a refractive index range ( $\Delta n$ ) as high as 0.22<sup>5</sup>, while that in a human eye is typically 0.03<sup>6</sup>. Harnessing S-GRIN brings a new type of optical element for the first time since the introduction of holographic optical elements some 35 years ago. Fundamentally, new materials open alternate horizons for innovation. S-GRIN lenses have already been introduced in applications such as laser beam shaping<sup>7</sup>, achromatization with S-GRIN singlets<sup>8</sup> that enable lightweight disposable spaceborne optics and new classes of surgical glasses. The S-GRIN process has resulted in the fabrication of a historically intriguing Luneburg lens<sup>9</sup>, which is spherically symmetric and concentrates all incoming light to one or more focal points enabling fiber coupling<sup>10</sup> and high-concentration solar collection<sup>11</sup>. Overall, S-GRIN components provide new prospects for lightweight and broadband management of light, particularly once the processes are in place for providing high quality optical components.

GRIN optical components have historically fallen short of theoretical expectations due to an inability to create a significant  $\Delta n$  ( $>0.05$ ) through a significant volume ( $>10$  mm diameter, approaching 30 mm). A process to produce nanolayered polymer film based S-GRIN optical components with unparalleled control and range of refractive index distribution throughout an unprecedented volume has been developed at Case Western University<sup>12,13</sup>. This fabrication process, based on nanolayer coextrusion of polymer film processing, is capable of producing polymer films comprised of 4097 nanolayers with individual layer thicknesses below a quarter-wavelength of visible light<sup>14,15</sup>. These composite nanolayer films are created in a controlled series, 50 microns thick, forming part of a library of films each representing a specific refractive index. Each film is manufactured with an incrementally higher (or lower) refractive index in steps as small as 0.00082 spanning the range from 1.4898 to 1.5727 at 632.8 nm. The refractive index of these thin films takes on a value that is predicted by effective medium theory<sup>16,17</sup>. The refractive index is adjusted by controlling the fractional contribution of two (and in the future more) raw materials, each with substantially different refractive indices that are known to be polymerically compatible, entering the film coextruder. In the manufacturing of optical components, the extruded nanolayered films are then stacked and thermopressed to create a consolidated GRIN sheet of hundred films. The sheet is then further processed into a preform yielding an S-GRIN that is diamond turned into a final optical component.



Optical Coherence Tomography (OCT)<sup>18,19</sup> is an imaging technique that is capable of non-destructive and non-invasive three dimensional (3D) depth sectioning of biological samples at high resolution and high speed. The capability of OCT for noninvasive measurement of the refractive index profile of a crystalline lens has been demonstrated before. For instance, Verma et al. demonstrated extraction of the radial GRIN profile of fisheye lenses using 3D OCT data and a numerical ray tracing algorithm<sup>20</sup>, where measurement accuracy in refractive index of  $10^{-2}$  was reported. In addition, De Castro et al. report the reconstruction of the 3D GRIN profile of first a porcine crystalline lens *in vitro* using 3D OCT imaging, ray tracing, and a global search algorithm<sup>21</sup>. The method was based on the retrieval of the GRIN profile from the optical distortions produced on the posterior surface of the lens by the anterior surface and the GRIN. A precision in the GRIN reconstruction of  $4 \times 10^{-3}$  RMS was reported. The technique was later applied to *ex vivo* measurement of the GRIN profile of *ex vivo* human crystalline lenses to study the dependence of the GRIN profile with age<sup>22</sup>.

In this paper, as a path to understanding and resolving the remaining impediments to achieving the intriguing theoretical limits of GRIN imaging put forth by among others Luneburg<sup>9</sup>, we demonstrate the innovative application of OCT, with advanced methods<sup>23–28</sup>, to enable nondestructive metrology throughout the process of taking the nanolayered polymer films and turning them into the new form of S-GRIN optical components with unique optical correction for use in advanced lens systems. The database that is collected in a 3D scan of the evolving optical component provides information on the manufacturing process that is well beyond

detection by any other method, including direct observation or even conventional optical interferometry. The resulting precise map of the internal material architecture in 3D, whose structures are differentiated by optical path differences created by the layered films as well as by potential scatter sources from residual process impurities, allows the manufacturer to refine the manufacturing process to achieve diffraction limited S-GRIN components. Unlike a conventional optical component, where the refractive index is assumed to be uniform throughout the component, in creating a S-GRIN component it is the 3D index distribution that defines the lens architecture. As an enabling technology, OCT inspection is readily accomplished ahead of the highest step in creating the component value; the diamond turning of the optical surfaces. Visually, throughout this process of creating the optical component with a S-GRIN distribution, the collection of nanolayered films appears fully transparent even though it is made of a stack of hundreds of polymeric films.

## Results

Figure 1 illustrates the process that creates an optical component S-GRIN lens. An intermediate component, known as preform, is equivalent to the state of a traditional glass lens blank after the radii of each surface have been generated, but before polishing. The process described here is the first to enable a direct path to a S-GRIN lens<sup>29</sup>. In addition, this process currently enables  $\Delta n$  as large as about 0.08 over a diameter of 30 mm, with emerging  $\Delta n$  of 0.17. Previously, radial and axial gradients have been the only forms that have been successfully manufactured<sup>30</sup>. The prior art in these forms of GRIN lenses has been mainly limited to a diameter under 5 mm and a  $\Delta n$  of 0.02. In

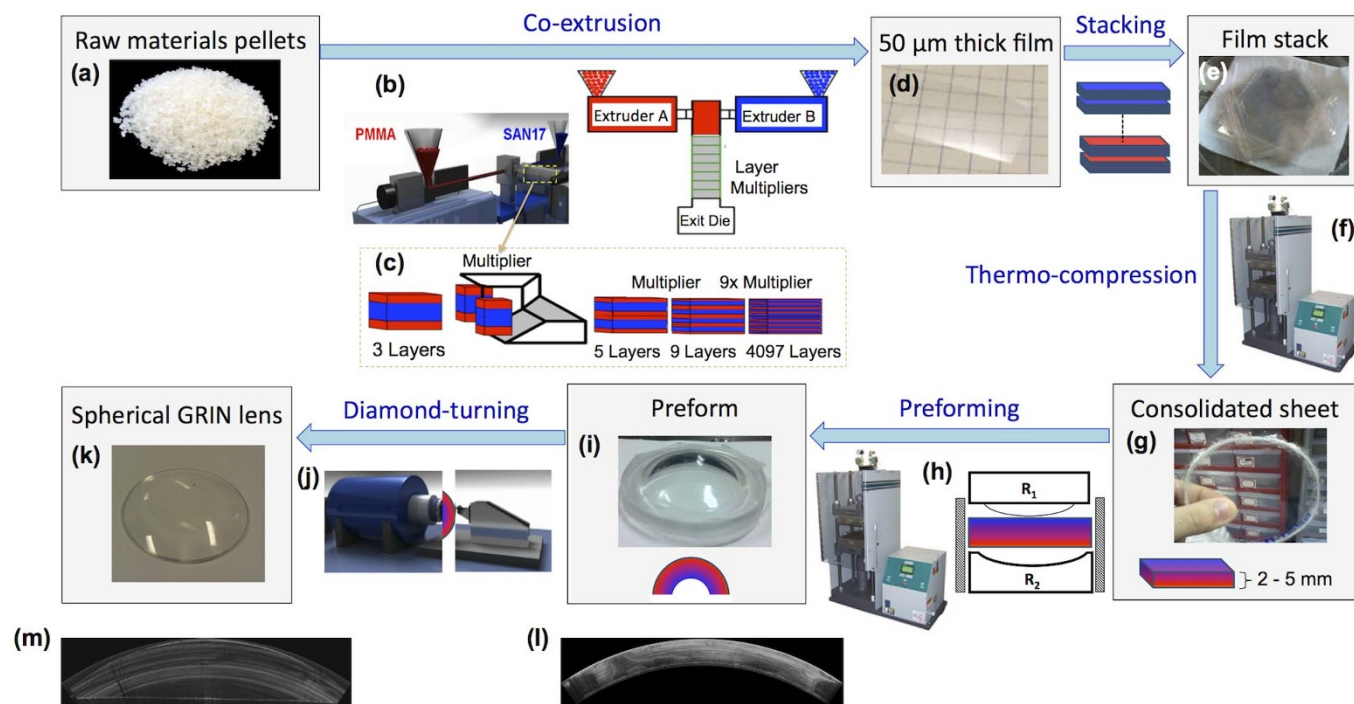


**Figure 1** | A flow chart of fabrication process of S-GRIN. Starting at (a), up to three raw materials (two shown at (b)) are fed as pellets into the funnels where they melt and then pass through a 12 stage splitter (c) resulting at the output (d) in a continuous 350 mm wide roll of 50  $\mu\text{m}$  thick film comprised of 4096 fully transparent nanolayers, which resembles Saran Wrap. Each roll of film has a specific, constant refractive index, measured with a Metricon to 0.001; 51 individual rolls may be made with increment in index and placed in bins of refractive index between the lower index, PMMA (1.48981) and in this case SAN 17 (1.57266) at 632.8 nm. To reach (e), based on a gradient distribution from the optical designer, a loose stack of the 50  $\mu\text{m}$  films is made using oversized film squares by extracting the films from their refractive index bins. This stack of about 50 films is then thermopressed in (f) at 125°C and 17,000 lbs pressure to create what represents the raw GRIN material consolidated sheet, shown at (g). The next step (h) creates the GRIN preform (i), the equivalent of a lens blank bended so both surfaces have initial radii. OCT pre-inspection can occur both at the compressed sheet level (g) and after the creation of the preform for the diamond turning process (i). The final step in the process is diamond turning (j) the preform (i) to create the finished lens (k). Using a custom OCT with rotation stages in the sample arm for angular scan, the internal images of a preform and a lens shown at (l) and (m) respectively have been obtained.



addition, the S-GRIN form enables correction of optical aberration types that are not addressed by the prior forms of GRIN<sup>31</sup>.

The process of coextrusion from two polymers involves a patented replicator that creates  $2^{12} + 1$  or 4097 layers less than  $\frac{1}{4}$ -wave thick using 12 identical replicators<sup>32</sup>. The output from the coextruder is a continuous film, resembling “Saran Wrap” that is 0.3 meter wide and typically many meters long. By precisely adjusting the fractional material mix into the coextruder, the refractive index of the film is controlled. To reduce the impact of particulate contamination, a cover layer is added as the film emerges, which is peeled off when the various films are stacked to construct a GRIN sheet. The two materials are currently a combination of polymethylmethacrylate (PMMA Plexiglas V-920, Arkema Inc.) and a copolymer of styrene and acrylonitrile (SAN17, Lustran Sparkle, Ineos, Inc.). In the next step, based on a S-GRIN prescription, a set of typically hundreds of these unique refractive index films are taken from the appropriate nearest bin in the film library and stacked into the prescribed distribution of refractive index versus depth. The stack of films is then thermopressed into a sheet that is planar on both sides. At this stage, in anticipation of the final diamond-turning step, and to reduce edge effects from the compression, a few tens of what will become sacrificial films are added on each side of the sheet. An OCT based inspection of the sheet is conducted as the final step on the sheet in advance of creating the preform, whose bend radius is an optical design parameter that is independent of the actual radii that will be the outer surfaces of the optical component. It is also most leveraged to use the OCT system to inspect the preform in advance of the diamond turning of the optical surface, which is the process step that is at the peak of the component value creation curve. Primarily because this optical component manufacturing process is based in polymer materials, it is essential that a continuous nondestructive metrology method with micron-scale resolution be provided to ensure high performance.

There are a series of fundamentally different implementations of OCT<sup>33</sup>. In this paper, we focus on two OCT methods we applied to the metrology of GRIN materials. One of the two OCT methods is a method we developed in our laboratory, Gabor-domain optical coherence microscopy (GD-OCM), that uniquely provides 2  $\mu$ m resolution in both the axial (Integral, Femtolaser Inc.) and the lateral dimensions throughout up to 2 mm of a component (i.e. with custom optics and algorithms)<sup>23–25,34–37</sup>. Starting with the 3D imaging of individual polymeric films, the GD-OCM microscope enabled the investigation of 50  $\mu$ m thick polymer films of extruded SAN17/PMMA (#030111 and #081511) bounded by 25  $\mu$ m thick protective layers on either side. Two films were of the same composition, yet processed under different protocols in terms of the temperature and the pressure applied during manufacture. With 2  $\mu$ m resolution, minuscule line and particle defects on the scale of a few microns were clearly identified inside the films. Furthermore, the locations and dimensions of the defects in 3D were precisely measured.

Figure 2(a,b) shows 3D GD-OCM imaging of two films rendered by Voxx software (The School of Medicine, Indiana University). Film #081511 exhibits densely distributed defects, compared to film #030111, as shown by an ocean of particulates across the entire film volume. Figure 2(d,e) are two examples of enlarged *en face* and corresponding cross-sectional images of a few typical defects of film #030111 as denoted by red arrows in Fig. 2(b). The lateral extent of the defects can be identified and quantified from the *en face* images whereas their depth locations and extent can be accurately quantified from the cross-sectional images. A discovery based on this first of its kind metrology was that, for otherwise equivalent films, the temperature and pressure used in the processing created more or fewer defects in the films. In addition, a 1000  $\mu$ m  $\times$  1000  $\mu$ m  $\times$  650  $\mu$ m portion of a polymeric GRIN sheet (i.e. component #A2-2) from the top surface was imaged using GD-OCM to inspect the internal structures of the stacked films in a sheet, as shown in Fig. 2(f). The minuscule line and particle defects as well as the boundaries of the

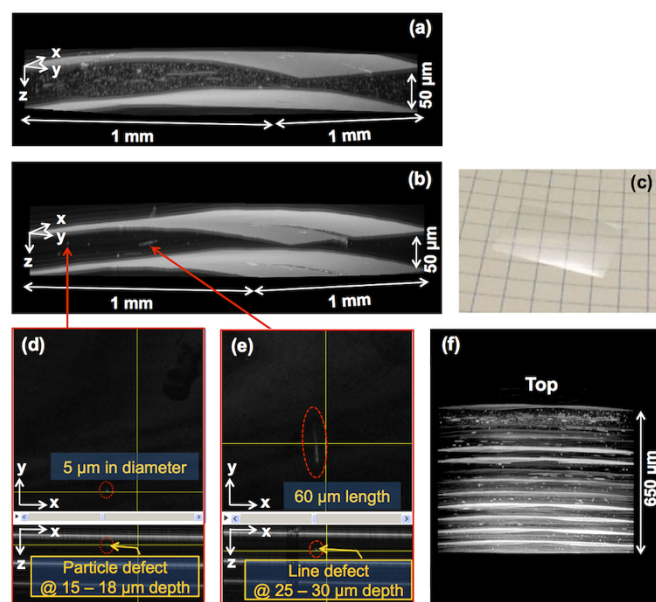


**Figure 2 |** GD-OCM imaging of two identical composition 50  $\mu$ m films thermopressed under different temperatures and pressures and a GRIN sheet. (a) film #081511 showing a multitude of defects. (b) film #030111 showing few defects (c) Photograph of a 50  $\mu$ m thick film. (d–e) two examples of enlarged *en face* and corresponding cross-sectional images of a few typical defects of film #030111 in the locations denoted by red arrows in (b). (f) Snapshot of volume-rendered 3D image obtained by GD-OCM when light was incident through the top surface of GRIN sheet.

films in the GRIN sheet are clearly resolved across an extended depth of focus of 660  $\mu$ m with 2  $\mu$ m lateral resolution.

The second of the two OCT methods applied to the metrology of GRIN materials is Swept-Source Fourier-domain OCT (i.e. SS-OCT)<sup>26,38</sup>, with two custom features; a swept source centered at 1320 nm spanning a bandwidth of 158 nm at 45Khz sweep rate<sup>27</sup> and a dual detection scheme<sup>28</sup>, a novel hardware solution for mirror image suppression developed in our laboratory. The source imposes 8  $\mu$ m axial resolution, and the optics (LSM03, Thorlabs) operates in telecentric mode at up to 20  $\mu$ m lateral resolution at full aperture that is maintained over a 0.6 mm depth-of-field in the component under test. It should be noted that the high resolution of GD-OCM (i.e. 2  $\mu$ m laterally and axially as compared with 20  $\mu$ m laterally and 8  $\mu$ m axially of SS-OCT) is tailored to imaging composite films with thickness of about 30 to 100  $\mu$ m and stack of composite films up to 2 mm thick, where the visualization of minuscule lines and particle defects within the film is critically sought. Nevertheless, the high resolution advantage of GD-OCM comes with the cost of limiting the imaging field of view (i.e. 2 mm  $\times$  2mm laterally) and depth (i.e. up to 2 mm axially); hence GD-OCM is not suitable for imaging the whole volume of GRIN sheets, which are typically about 25 mm  $\times$  25 mm in aperture size and 5 mm or more deep. Given that SS-OCT is operated in a region around the wavelength of 1300 nm, its axial and lateral resolutions are relatively lower than GD-OCM, while gaining larger scanning FOV (i.e. 30 mm  $\times$  30 mm) and imaging depth range (i.e. more than 5 mm). As a result, SS-OCT is tailored to imaging the whole volume of a typical GRIN sheet, particularly at high speed. With SS-OCT, we demonstrate for the first time, the nondestructive metrology of nanolayered polymer S-GRIN optical components, specifically the 3D structural profiles of the thermopressed films in the sheet shown in Fig. 3, and/or preform prior to final shaping by diamond turning. One depth scan (also referred to as an Axial scan or A-scan) produces 400 samples with a sampling resolution of 1.9  $\mu$ m. A single 3D dataset consists of 1250 frames

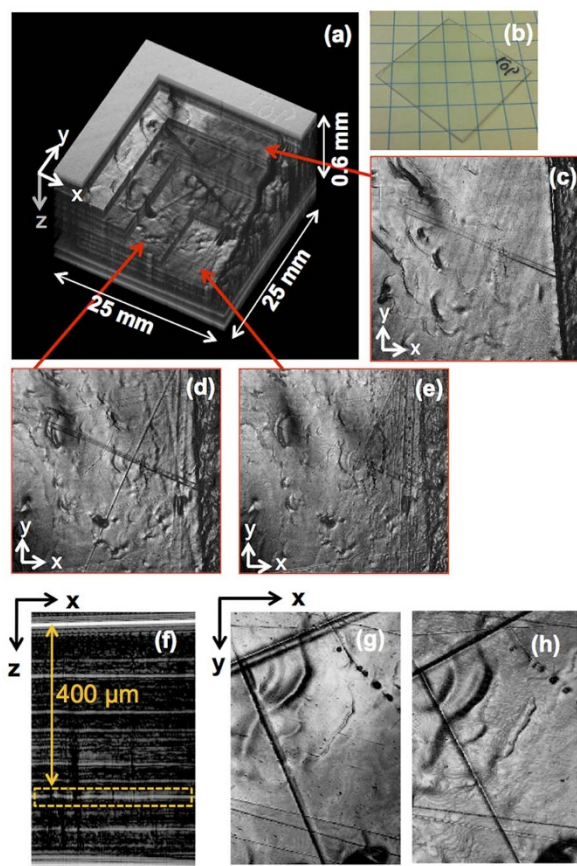


**Figure 3 | Nondestructive 3D OCT imaging of a thermopressed GRIN sheet manufactured with stacked films each tens of microns thick before compression, where each film is made of hundreds of nanolayered films.**

(a) An example of volumetric rendering of 3D structural data obtained by OCT imaging. The 3D rendering was virtually sectioned in plateaus to show internal topography at different film layers within the sheet. (b) A photograph of the thermopressed stack of hundreds of nanolayer films comprising the GRIN sheet used for all the frames, which is visually transparent without distinguishable optical distortion. (c–e) Examples of representative *en face* reconstructions from the acquired 3D OCT data showing individual embedded film topography at different depths inside the sheet. (f) A 2D cross sectional image of the GRIN sheet, where the first bright horizontal line corresponds to the strong reflection at the top surface of the sheet and subsequent lines correspond to relatively weak reflections from each consecutive internal film interface, where the index increments by 0.0015. (g–h) *En face* reconstructions at the depth position indicated by a yellow dash box when beams were incident from (g) the top and (h) the bottom surface of the sheet, respectively; the topography of an individual film, which is bounded by films with one unit increment in refractive index (currently 0.0015), is unaffected by the intervening GRIN material.

with 1500 A-scans per frame, corresponding to a lateral FOV of  $25 \times 30 \text{ mm}^2$  when laterally sampling every  $20 \text{ }\mu\text{m}$ . This level of sampling enables constructing a database of the internal optical quality that encompasses low and mid-spatial frequency content.

Figure 3(a) shows a screen capture of a 3D reconstruction created from OCT data rendered with Voxx software. The data were collected from a sheet created at PolymerPlus by thermopressing a stack of hundreds of the 50-micron thick (before thermocompression) nanolayered films. The depth dimension (*z*-axis) is expanded to illustrate the capability of OCT to image at micron-level depth resolution and the resulting ability to resolve sub-surface layer structure in what appears to be a fully transparent, homogeneous optical window. Figure 3(b) is a photograph of the GRIN sheet, indicating that

no visible residual of the layering process is evident. Figure 3(c)–(e) illustrates a set of reduced *en face* images obtained from summation of 10 *en face* images (*x*-*y* plane) of the raw 3D dataset at *z*-depths of  $160 \text{ }\mu\text{m}$ ,  $380 \text{ }\mu\text{m}$ , and  $450 \text{ }\mu\text{m}$ , respectively. OCT enables the non-destructive visualization of the internal topography of the layered GRIN sheet. This information is crucial to the successful volume manufacture of S-GRIN optical components, a first in science. All *en face* images were generated using the ImageJ software (National Institutes of Health). Figure 3(g,h) show two *en face* images extracted from the same film located approximately  $400 \text{ }\mu\text{m}$  below the front surface of the sheet as indicated in Fig. 3(f). These images were acquired from the top and bottom of the sheet, respectively. They show the same distribution of internal film topography with inversion of peaks and valleys as expected when imaging from the opposite sides of an internal 3D structure. This result demonstrates an important capability of OCT. The topography that is acquired and displayed is localized in the sheet. This is one of the unique, and in this application, enabling feature of OCT metrology. During the process of perfecting the manufacture of these new S-GRIN components, the 3D OCT imaging is used to guide the iteration of process temperature and pressure needed to create a nearly ideal topography at each of the film planes that often number more than 100. 3D OCT detects index differences as low as 1 part in  $10^6$  and, as a result, highlights subtle structures on a layer-by-layer basis<sup>39</sup>.

From a 3D dataset obtained by the SS-OCT system, the topography of the interface between any two consecutive internal film layers can be extracted by applying an appropriate segmentation algorithm. An efficient technique established empirically and illustrated in Fig. 4(b–e) is to acquire multiple, for example 500, scans at every *x*-*y* sampled point of the component and perform a fast Fourier transform of each spectrum before averaging over the 500 extracted profiles. A threshold for peak acceptance enables considering only peaks above a noise level. A window is then applied around each peak before quantifying the peaks location measured as the axial position of maximum intensity around the windowed interfaces. Mapping the axial position of the peaks across the lateral FOV yields the topography across the *x*-*y* plane of the targeted film interfaces. It should be noted that the measured optical path length (OPL) in OCT, corresponding with the location of an envelope's peak, is related to the group refractive index ( $n_g$ ) as opposed to the phase refractive index ( $n_p$ ) at the operating wavelength<sup>40</sup>. The measured optical path lengths and refractive indices can be scaled for other wavelengths through the well-known dispersion relation,  $n_g(\lambda_i) = n_p(\lambda_i) - \lambda_i (\partial n_p(\lambda) / \partial \lambda)_{\lambda_i}$ , where  $(\partial n_p(\lambda) / \partial \lambda)_{\lambda_i}$  is the dispersion slope at an arbitrary wavelength  $\lambda_i$ . This dispersion slope may be estimated by first measuring separately the phase refractive indices of each source material (i.e. PMMA and SAN17 in this case) at multiple wavelengths. Then a curve-fitting algorithm may be applied to obtain the dispersion curve across a wide spectral range. The dispersion curve of the composite material has been experimentally validated to be a linear combination of the two dispersion curves of the source materials.

The topography of the interface between two internal film layers not only allows visualization of the optical flatness of the internal film interface but also quantification of transverse optical quality of a group of films within the sheet after the compression process. For a given dataset of topography of the internal film interfaces, subtracting two consecutive interfaces yields a group optical thickness across the lateral plane as illustrated in Fig. 4(f). In each topography, the range of all color bars (i.e. from blue to red) is  $10 \text{ }\mu\text{m}$  and the green color corresponds to a mean optical thickness,  $n_g L$ , of the indicated layer. In the particular sheet examined, a typical optical thickness variation, as specified by a standard deviation across the *xy*-plane, is measured to be about  $0.6 \text{ }\mu\text{m}$  over a  $200 \text{ }\mu\text{m}$  thick layer, which is about 0.3%.

As part of a controlled experiment, we performed 3D SS-OCT imaging on a polymeric GRIN sheet (i.e. component #A2-1), whose

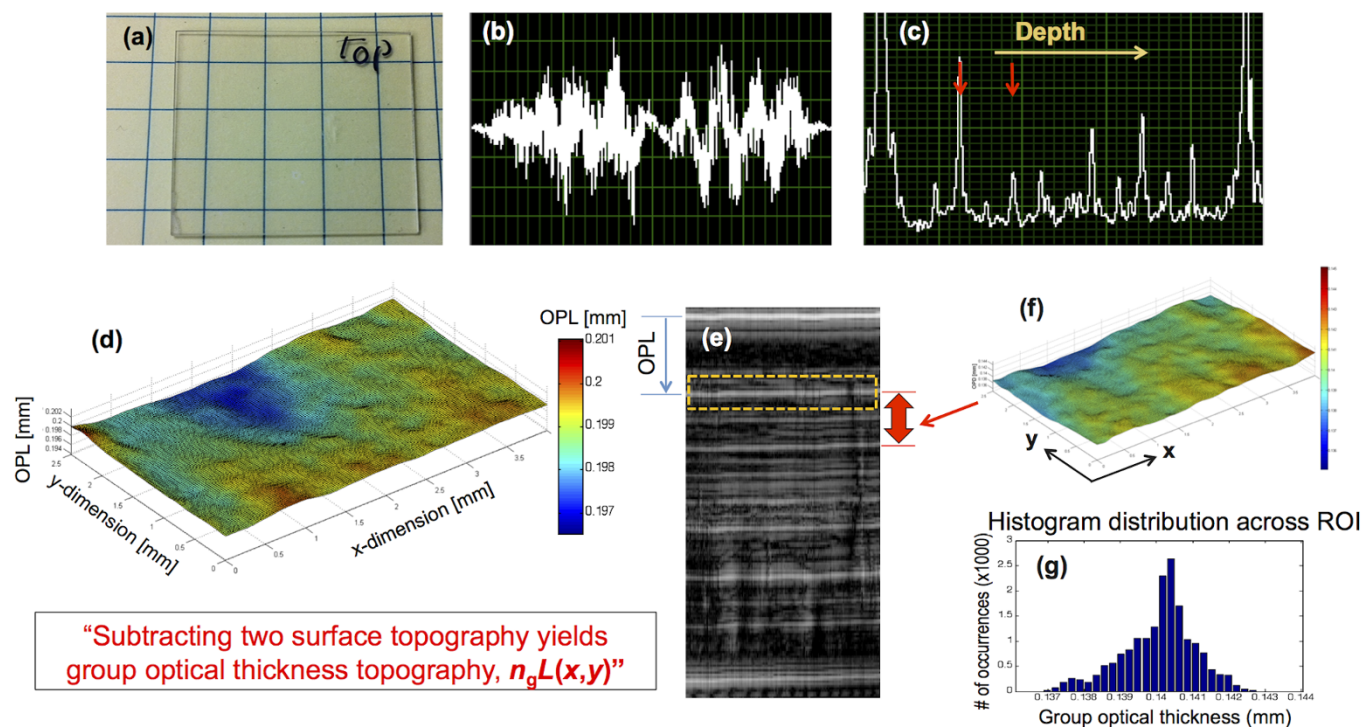


**Figure 4 | Interface and thickness topography of the layered GRIN polymer.** (a) A photograph of a layered polymeric GRIN sheet made of stacked thermocompressed films, which visually appears transparent. (b) An example of a spectral fringe at one  $x,y$  location of the sheet. (c) A depth profile obtained from taking the Fourier transform of the spectral fringe in (b). The red arrows indicate the two intensity peaks on the depth profile that correspond to the top and bottom surfaces of a two-films layer analyzed in (f). (d) An example of the topography of the interface circled in a yellow dashed line in (e). (e) A cross-sectional image of the sheet. (f) Topography of the optical thickness between two consecutive films denoted by a red double arrow in (e), revealing a micro-elevation map of the films interface after compression into the preform. (g) A histogram distribution plot associated with the thickness topography in (f), reveals and quantifies transverse inhomogeneity of the internal films thicknesses after the compression process.

thermopressed stack of films of equal thickness and the associated refractive index distribution of the films measured at 632.8 nm is shown in Fig. 5(a). Sequentially, the topography of the internal films interfaces was performed for all interfaces that were revealed by SS-OCT imaging (Fig. 5(b)). By subtracting the locations of consecutive interfaces, an optical thickness associated with group refractive index of each internal film layer beneath the component surface was obtained. Given prior knowledge of the material composition, i.e. the ratio between the PMMA and SAN17 and the refractive index dispersion of each material, the group refractive index at the imaging wavelength of 1320 nm was estimated for each film. The physical thickness of each film layer was then extracted as shown by a blue plot in Fig. 5(c,d). Except for an edge effect the film thickness is rather constant in depth. Standard deviations of the film thickness across the lateral dimension of the acquired data vary from 0.22 microns (film #1) to 2.43 microns (film #22), and are on average  $\sim 0.9$  microns. The thickness measurements were confirmed by a destructive test performed by cutting the sheet, polishing the cut surface, and imaging it under a light microscope with  $20\times$  magnification as shown in Fig. 6(a,c). The film thicknesses measured from the microscope image and that measured by SS-OCT over the same region of the polymeric sheet are plotted in Fig. 6(b) for the top part and Fig. 6(d) for the bottom part, which shows good agreement between the two measurement datasets. Therefore, OCT is revealed to be a compelling technique for non-destructive characterization of the layer distribution in layered polymeric material sheets in spite of their apparent full visual transparency. Given the good agreement between OCT and microscopy measurements, the group refractive indices and the phase refractive indices estimation at the 1320 nm operating wavelength as shown in Fig. 5(e) is within good accuracy. As a result, at the current state of fabrication of the polymeric layered

GRIN, the gradient index profile of the component would be ambiguous by the non-uniformity of internal films thicknesses across the sample. As part of our future work, a protocol to simultaneously extract both refractive index and thickness of internal film is under investigation.

## Discussion

The technology of fabricating nanolayered polymer materials enables an unusually large ( $\Delta n \sim 0.08$ ), continuous user-defined refractive index and dispersion intermediate to the bulk materials that are used in creating the films. This nanolayered film is a key component that leads to fabrication of the first true spherical gradient distribution GRIN lens or S-GRIN optical component. Prior GRIN lenses have been restricted to radial and axial gradients only. These S-GRIN lenses provide to optical system designers a new optical component, with unique aberration correction properties, an event that is rare in the history of lenses and lens design<sup>8,12,13,31</sup>. Nevertheless, this new type of nanolayered material also leads to a unique characteristic that is not compatible with any traditional metrology tools and hence requires development of a new type of metrology to enable high quality of the layered S-GRIN optical components.

We have developed OCT-based techniques of subsurface inspection applied to S-GRIN lenses to visualize the stages of enabling and perfecting the manufacture of these optical components. The most revealing visualizations that are presented are based on a recent breakthrough in three-dimensional subsurface imaging; GD-OCM. It should be pointed out that the OCT field is currently quite dynamic with many variants being academically and commercially developed. However, it should be noted that all OCT/OCM methods other than GD-OCM have lateral resolution that is limited to no better than

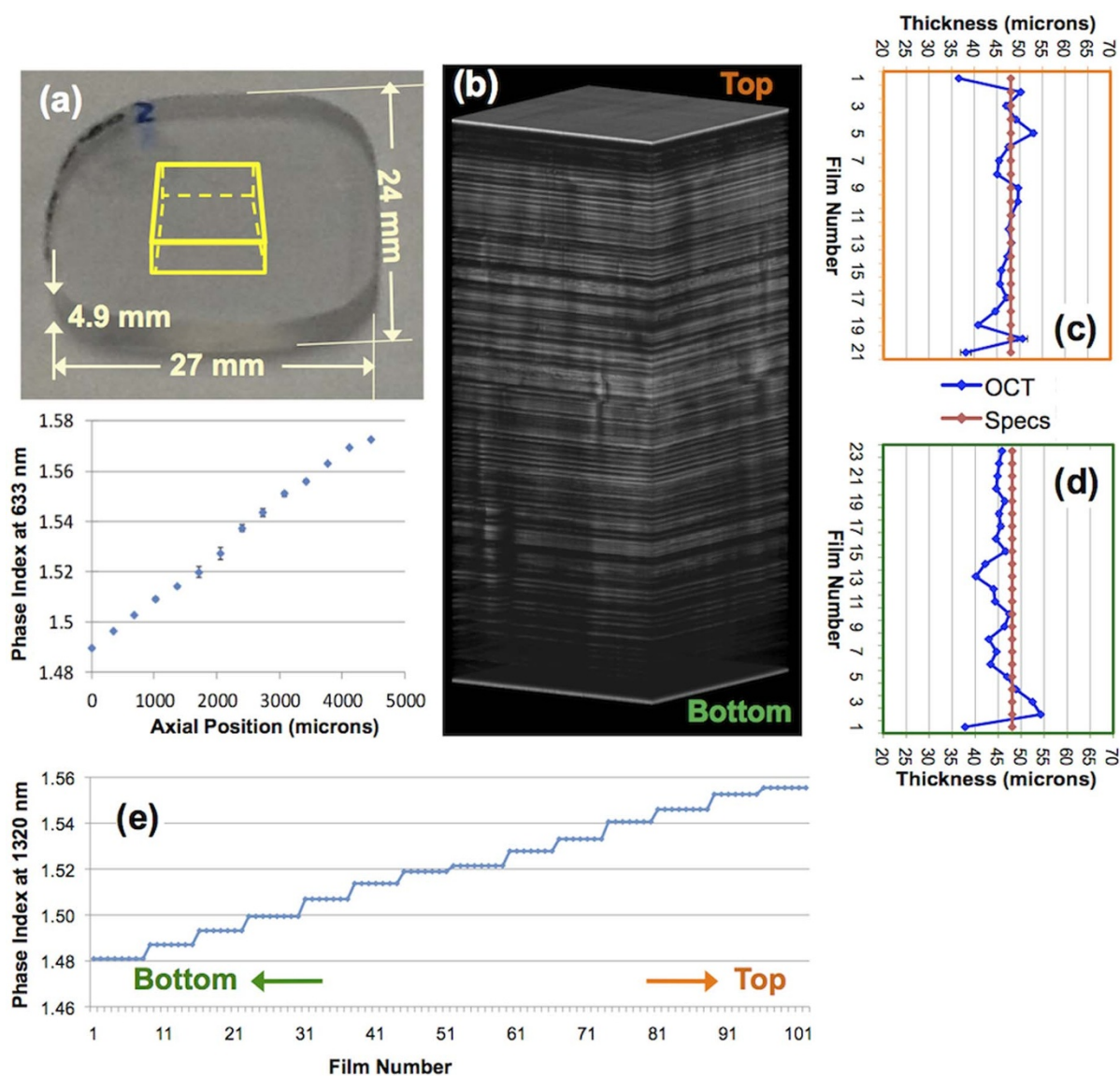


**Figure 5** | Non-invasive determination of the films thickness distribution of a PMMA/SAN17 GRIN sheet. (a) A photograph of the GRIN sheet under test (top) and the associated refractive index distribution measured at 633 nm (bottom). (b) is a volumetric rendering of the 3D dataset obtained by SS-OCT when light was incident through the top surface of the sheet. (c) and (d) are films thickness profiles (in red) nominal and (in blue) extracted from the top and bottom portions of the dataset in (b), respectively. (e) is the estimation of the gradient refractive index profile at 1320 nm wavelength, across the 102 films of the sheet.

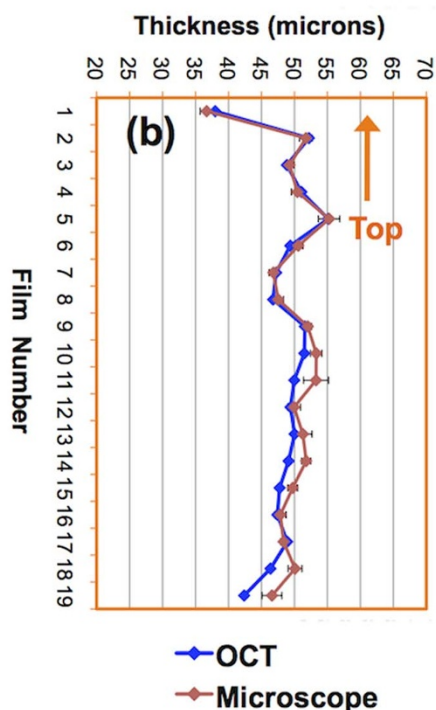
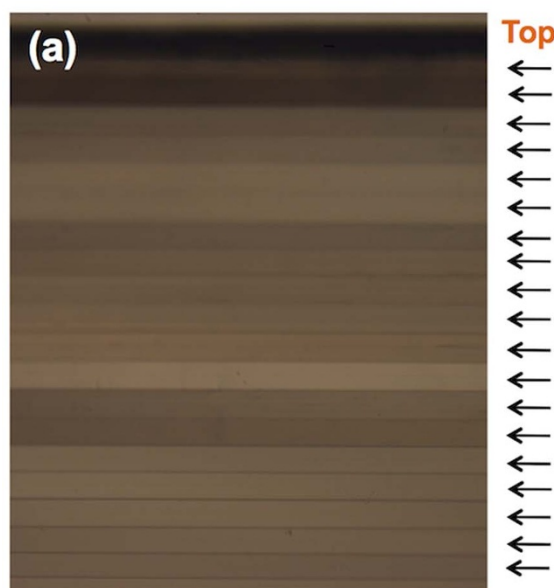
about 10 microns and often 20 microns. Moreover, lateral resolution numbers are rarely reported through a volumetric depth, i.e. only the resolution at the focal plane is usually reported. The capability of GD-OCM to image at 2  $\mu\text{m}$  resolution in 3D allowed the polymeric GRIN component quality to be substantially improved at the film level. This nondestructive 3D metrology is useful to optimize the manufacturing parameters and to screen and diagnose films during manufacturing to yield high-performance optical films, then sheets, and finally preforms. Moreover, the SS-OCT imaging of the GRIN component immediately provides information about its 3D internal topology that is beyond direct visibility and in many cases beyond what an interferometer would detect. This topology data allows the manufacturer to immediately evaluate whether the latest iteration on the manufacturing process, which may involve a new batch of raw materials and typically involves adjustment to the temperature and/or pressure during thermopressing, has resulted in an improvement, as a basis for selecting the parameters for the next iteration, if any. The films-interface topography not only provides information about

internal film deformation but it can also be used to determine the transverse optical thickness distribution of each of the film layers across the component. The information can be fed back into the manufacturing process to optimize the compression error of the mold to improve the fabrication of high precision optical components.

It should be pointed out that the proposed technique is applied not only to a sample with flat parallel surfaces, such as the GRIN sheet, but also a sample with curved surfaces, such as GRIN lenses or spherical GRIN shells, with modification of the sample probe and scanning scheme. A first issue that causes challenge in 3D OCT imaging of curved GRIN preforms as compared with GRIN sheets is that the conventional OCT scanning, such as that used in imaging of sheet samples, tend to lose penetration as soon as we scan over a 1 mm lateral scanning FOV. This is simply because most of the incidence power is reflected out of the collecting numerical aperture of the objective lens at the outer surface of a curved preform if the incident angle is far apart from the normal incidence angle. To



### Top part under light microscope



### Bottom part under light microscope

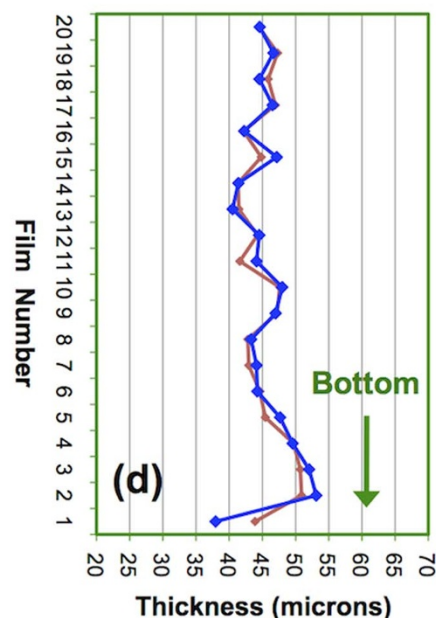
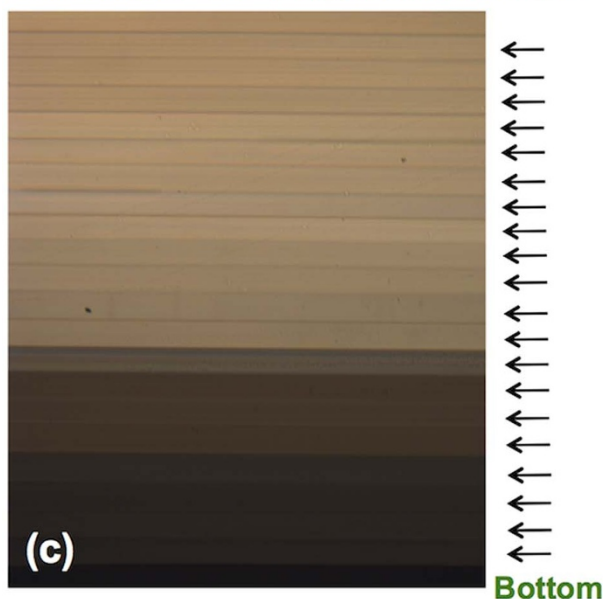
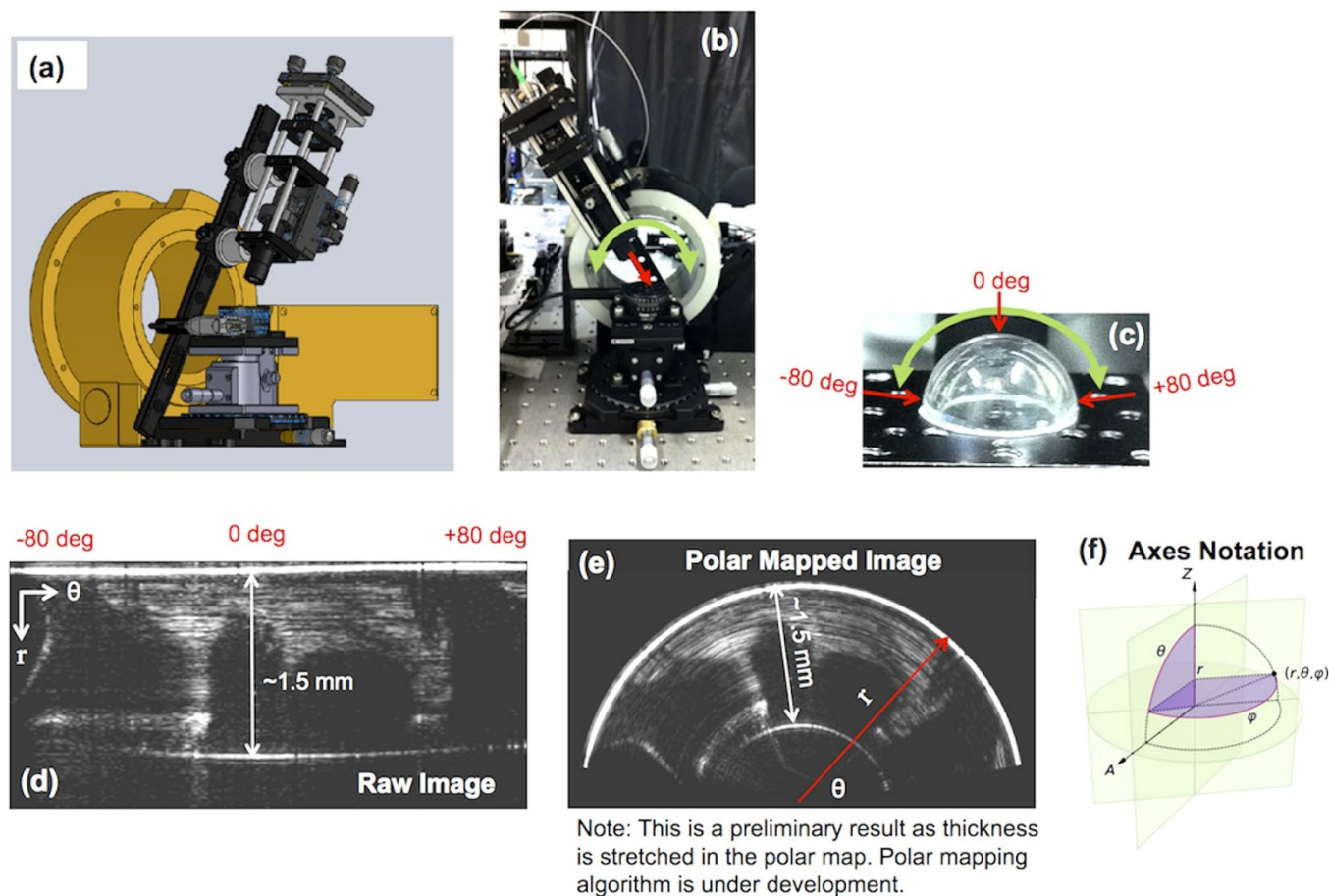


**Figure 6** | Comparison between thickness data obtained by SS-OCT (non-destructive) and light microscopy (destructive). (a, c) are cross-sectional images of the top and bottom parts, respectively, of the polymeric sheet component obtained by light microscopy. (b, d) are film thickness distribution of the top and the bottom parts, respectively, measured by both SS-OCT and light microscopy.

remedy this issue, we adopted a scanning scheme where the incident beam is ideally always normal or close to normal while acquiring 3D OCT data of a curved preform. This scanning pattern is achieved by designing the beam-scanning path to follow the outer curvature of the sample by using a combination of two rotational motorized stages as illustrated in Fig. 7(a, b). Note that only the sample scanning head was modified and, therefore, it is possible to design a single OCT system that is interchangeable between imaging of a GRIN parallel plate and a GRIN curved preform by switching the sample arm (mechanically or optically). Moreover, as part of our preliminary experiment, we performed angular OCT imaging of a GRIN

Luneburg's outer shell that has a shape of half a sphere as shown in Fig. 7(c). The developed system allows cross-sectional imaging across full aperture of the half-sphere Luneburg's outer shell as shown in Fig. 7(d) for the raw data and Fig. 7(e) after applying polar mapping. Fig. 7(f) shows notation of the scanning axes. In this preliminary result, the deformation of the bottom medium-air interface as compared with that of the top surface is clearly observed and indicates non-concentricity of the shell. Using the obtained OCT data, the edge thickness was determined to be about 6% thinner than the center thickness (i.e.  $\sim 1.56$  mm at the center and  $\sim 1.47$  mm at the edge). In addition, for convex-convex lenses, raytracing methods



Note: This is a preliminary result as thickness is stretched in the polar map. Polar mapping algorithm is under development.

**Figure 7** | Layout of the angularly-scanning sample arm and preliminary SS-OCT imaging result of a GRIN Luneburg's outer shell. (a–b) are 3D illustration and actual photograph of the angularly scanning sample arm. (c) is a photograph of a GRIN half-sphere Luneburg's outer shell. (d–e) are OCT images of the shell acquired directly by the system and after post-processing of polar remapping, respectively. (f) demonstrates the notation of the axes used in (d–e).

as exemplified by De Castro et al.<sup>21,22</sup> may be combined with the modified scanning scheme in order to, in the future, estimate the GRIN profile.

In summary, it is evident that the ability to visualize and quantify the 3D internal structure of nanolayered polymer films and layered GRIN polymer at micrometers scale is a leap forward for the optimization of the fabrication process, particularly when manufacturing high quality and precision grade optical components, where long term and continuous monitoring is required. An ultimate goal of this on-going research is to non-destructively also extract 3D refractive index profile of the layered GRIN polymer. The challenge arises by the fact that, in practice, both refractive index and physical thickness of the internal films are unknown. As a result, a technique of high precision simultaneous measurement of the phase refractive index, the group refractive index, and the thickness of each film layer is under active investigation<sup>41–44</sup>.

## Methods

**Layered GRIN polymers fabrication.** A manufacturing process to produce nanolayered PMMA/SAN17 films with an unparalleled control of the internal refractive index distribution has been previously described<sup>1–4</sup>. Consolidated GRIN polymer sheets were fabricated through a process of thermoforming a series of stacked nanolayered PMMA/SAN17 films of varying index for non-destructive evaluation with the OCT equipment characterization capabilities. Unique consolidated sheets, one being shown in Fig. 5(a), were prepared for OCT analysis. A GRIN sheet designated #081511-A2-1, consolidated 102 individual polymer films with a linear refractive index gradient of magnitude 0.08, varying from 1.4898 to 1.5727, through the 4.9 mm sheet thickness. The GRIN sheet was constructed as stacks of nanolayered PMMA/SAN17 films, each 50 microns thick. The film stack

was consolidated to the target sheet thickness between stainless steel plates at 125°C under 17,000 lbs in a heated hydraulic laboratory press. 24 mm × 7 mm × 4.9 mm sections were cut from the compressed sheet and transmitted for characterization by OCT.

**Gabor domain optical coherence microscopy (GD-OCM).** GD-OCM is a type of spectrometer-based Fourier Domain OCT<sup>38</sup> developed in our laboratory<sup>23</sup>, which has demonstrated unprecedented lateral resolution in skin<sup>36,37</sup>. The GD-OCM system utilizes a liquid lens embedded in a custom optical system designed to achieve dynamic focusing of the component at, unprecedented, both axial and lateral optical resolutions of 2 μm throughout up to 2 mm of a component<sup>23</sup>. As shown in a system's layout in Fig. 8(a), a broadband light from a Titanium:Sapphire femtosecond laser centered at 800 nm with 120 nm FWHM (Integral, Femtolasers Inc.) was divided into two arms of a fiber-based Michelson interferometer employing a broadband custom-made 80/20 fiber coupler (NSF-DARPA/PTAP); 80% of the light was focused on a component through a custom liquid-lens-based three-dimensional scanning objective<sup>24</sup> and the other 20% of light was delivered to the reference arm with a custom dispersion compensator, which is based on the principle of the Fourier domain optical delay-line<sup>34</sup>. Reflected or backscattered light from the component was interfered with light reflected from the reference arm and then detected by a custom spectrometer with a high speed CMOS line camera (spl8192-70 km, Basler Inc)<sup>25</sup>. The spectrum of the interference signal was registered onto 4992 pixels (10 μm × 20 μm per pixel) of the CMOS line camera through the spectrometer. The Fourier transform of the spectrum corresponds to a depth profile of the component reflectivity along the incident beam path. The exposure time was set to 20 μs and the acquisition speed was 23,000 A-scans/sec with x-y scanning by two cross-axes mirrors driven by two galvanometers synchronized to the acquisition of the CMOS camera. Given its 3D high resolution imaging capability, GD-OCM was used to study the characteristics of SAN17 extruded to form a 50 μm thick film placed within 25 μm clear protective layers. For the 3D imaging of the films at 2 μm resolution, light was focused at the center of the film by adjusting the applied voltage to the liquid lens embedded in the objective. The depth of focus 60 μm, which was assessed experimentally<sup>35</sup>, was sufficient to achieve 2 μm resolution over the 3D effective 50 μm thick film with one focus adjustment of the liquid lens. One A-scan consisted of 500 sampling points with

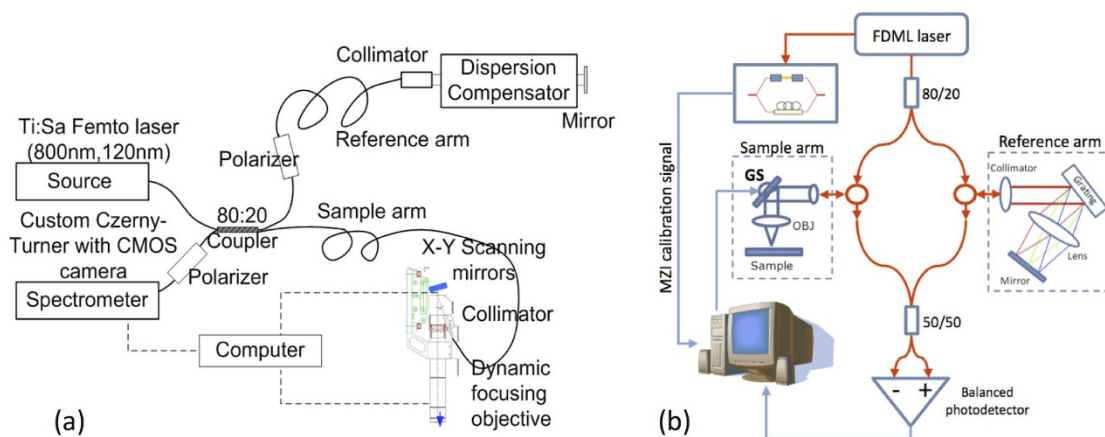


**Figure 8** | Layouts of the two OCT systems: (a) the GD-OCM system and (b) the SS-OCT system.

a depth sampling resolution of  $\sim 0.9 \mu\text{m}$ . An acquired 3D dataset of a film is comprised of 1000 frames with 1000 A-scans per frame, corresponding to a geometrical lateral FOV of  $1 \times 1 \text{ mm}^2$  with lateral sampling resolution of  $1 \mu\text{m}$ . For the GRIN sheet imaging, we acquired eleven volumes from the same  $1000 \mu\text{m} \times 1000 \mu\text{m} \times 650 \mu\text{m}$  portion of a GRIN sheet from the top surface with a sampling interval of  $1 \mu\text{m}$ , which corresponded to  $1000 \times 1000 \times 11$  A-scans or spectra. The eleven volumes were taken relative to shifted focal planes with  $60 \mu\text{m}$  separation to achieve  $2 \mu\text{m}$  resolution over the imaged portion of the GRIN sheet. The eleven volume images were reconstructed in post processing into one volume using the Gabor-based fusion technique<sup>23</sup>. All acquisition and post processing including interpolation, fast Fourier transform and fusion were done using Labview software based on 64 bit windows.

**The Swept-Source OCT (SS-OCT).** SS-OCT used in our experiments was a custom-built tabletop OCT system that utilizes either of two high-speed frequency-swept lasers. One swept source is a research prototype custom developed in 2008 in partnership with MicronOptics to be high speed and the largest bandwidth single semiconductor optical amplifier swept sources at  $1320 \text{ nm}$ <sup>27</sup>. The laser emits a quasi-monochromatic light (i.e.  $\sim 0.2 \text{ nm}$  linewidth) that is periodically swept over a wavelength range of  $1240 - 1400 \text{ nm}$  at a constant sweep rate of  $45,000$  cycles/second. All SS-OCT datasets were acquired and analyzed with the custom swept source other than the data shown in Fig. 5(b). The data in that figure was acquired using a Santec (HSL-2100-WR) swept source whose linewidth (i.e.  $\sim 0.1 \text{ nm}$ ) enables imaging the entire  $4.9 \text{ mm}$  depth of the sample at  $\sim 100 \text{ dB}$  sensitivity. A fiber-based Mach-Zehnder interferometer was implemented as illustrated in Fig. 8(b). Light from the laser was coupled into fiber, split by an 80/20 fiber coupler, and then delivered to the component and reference arms of the interferometer. Light in the component arm was focused into a component through the objective lens. Backscattered light from the component was then collected and recombined with light from the reference arm with a 50/50 coupler. The interference signal was detected by a balanced photodetector (model 1817, New Focus), digitized by a high-speed, 12-bit-resolution analog-to-digital converter operating at  $200 \text{ Msamples/s}$  (NI PCI 5124, National Instrument), and processed by a personal computer to construct a cross-sectional image of the component. It should be noted that the Fourier transform of a single interference spectrum yields an entire component reflectivity profile along the incident beam path. Combined with lateral scanning of the component beam, 2D and 3D cross-sectional images were obtained. Aiming for development of high precision metrology, field distortion cannot be tolerated. A focusing optics in the component arm was a  $5\times$  near infrared microscope objective (LSM03, Thorlabs) that was designed and optimized for uniform OPL across a  $9 \text{ mm}$  lateral scanning distance. Furthermore, to avoid field distortion intrinsic to dual axis galvanometer beam steering<sup>45</sup>, a combination between a single axis galvanometer beam steering (VM500, GSI Lumonics) and a high precision motorized linear translation stage (VA-25XA, Newport) was used to obtain 3D OCT data. The flatness of the imaging field as well as the lateral resolution of the system was verified by performing 3D imaging of the 1951 USAF resolution target (Edmund Optics). The optical lateral resolution was quantified to be approximately  $20 \mu\text{m}$ . Furthermore, a Fourier domain optical delay-line was implemented in the reference arm of the system to compensate for overall dispersion mismatch in the system<sup>34</sup>. The axial resolution of the system after dispersion compensation was measured to be  $\sim 8 \mu\text{m}$  for the MicronOptics source and  $\sim 10 \mu\text{m}$  for the Santec source. The depth of imaging of the system is limited by the spectral resolution of the laser source and was measured to be  $\sim 1 \text{ mm}$  in the case of the MicronOptics source and  $\sim 6 \text{ mm}$  in the case of the Santec source.

1. Gullstrand, A. *Helmholtz's treatise on physiological optics*. von Helmholtz, H. Southall, James P. C. edn (Optical Society of America: Washington, DC, 1924).

- Atchison, D. A. & Smith, G. Continuous gradient index and shell models of the human lens. *Vision Res.* **35**, 2529–2538 (1995).
- Moffat, B. A., Atchison, D. A. & Pope, J. M. Age-related changes in refractive index distribution and power of the human lens as measured by magnetic resonance micro-imaging in vitro. *Vision Res.* **42**, 1683–1693 (2002).
- Garner, L., Smith, G., Yao, S. & Augusteyn, R. Gradient refractive index of the crystalline lens of the Black Oreo Dory (*Alloctytus Niger*): comparison of magnetic resonance imaging (MRI) and laser ray-trace methods. *Vision Res.* **41**, 973–979 (2001).
- Jagger, W. & Sands, P. A wide-angle gradient index optical model of the crystalline lens and eye of the rainbow trout. *Vision Res.* **36**, 2623–2639 (1996).
- Berrigman, L. & Schaefer, C. *Optics of Waves and Particles* (de Gruyter: New York, 1999).
- Zahreddine, R. N., Lepkowicz, R. S., Bunch, R. M., Baer, E. & Hiltner, A. Beam shaping system based on polymer spherical gradient refractive index lenses. *Proc. of SPIE* **7062**, 706214 (2008).
- Beadie, G., Fleet, E. & Shirk, J. S. Gradient Index Polymer Optics: Achromatic Singlet Lens Design. in *Frontiers in Optics*. paper FThU5 (Optical Society of America, 2010).
- Luneburg, R. K. *Mathematical theory of optics*. 189–213 (Providence, Rhode Island: Brown University, 1944).
- Gabrielli, L. H. & Lipson, M. Integrated Gradient Index Luneburg Lens for Robust Fiber-to-Chip Coupling. in *CLEO: QELS-Fundamental Science*. paper QM1C.1 (Optical Society of America, 2012).
- Kotsidas, P., Modi, V. & Gordon, J. M. Nominally stationary high-concentration solar optics by gradient-index lenses. *Opt. Express* **19**, 2325–2334 (2011).
- Jin, Y., Tai, H., Hiltner, A., Baer, E. & Shirk, J. S. New class of bioinspired lenses with a gradient refractive index. *J. of Appl. Poly. Sci.* **103**, 1834–1841 (2007).
- Beadie, G. *et al.* Optical properties of a bio-inspired gradient refractive index polymer lens. *Opt. Express* **16**, 11540–11547 (2008).
- Ponting, M., Hiltner, A. & Baer, E. Polymer nanostructures by forced assembly: process, structure, and properties. *Macromol. Symp.* **294**, 19–32 (2010).
- Ponting, M. *et al.* Gradient multilayer films by forced assembly coextrusion. *Ind. Eng. Chem. Res.* **49**, 12111–12118 (2010).
- Kikuta, H., Yoshida, H. & Iwata, K. Ability and limitation of effective medium theory for subwavelength gratings. *Optical Rev.* **2**, 92–99 (1995).
- Haggans, C. W., Li, L. & Kostuk, R. K. Effective-medium theory of zeroth-order lamellar gratings in conical mountings. *JOSA A* **10**, 2217–2225 (1993).
- Huang, D. *et al.* Optical coherence tomography. *Science* **254**, 1178–1181 (1991).
- Fercher, A. F., Drexler, W., Hitzinger, C. K. & Lasser, T. Optical coherence tomography—principles and applications. *Rep. Prog. Phys.* **66**, 239–303 (2003).
- Verma, Y., Rao, K., Suresh, M., Patel, H. & Gupta, P. Measurement of gradient refractive index profile of crystalline lens of fish eye in vivo using optical coherence tomography. *Applied Physics B: Lasers and Optics* **87**, 607–610 (2007).
- de Castro, A., Ortiz, S., Gamba, E., Siedlecki, D. & Marcos, S. Three-dimensional reconstruction of the crystalline lens gradient index distribution from OCT imaging. *Optics Express* **18**, 21905–21917 (2010).
- de Castro, A. *et al.* Age-dependent variation of the gradient index profile in human crystalline lenses. *Journal of Modern Optics* **58**, 1781–1787 (2011).
- Rolland, J. P., Meemon, P., Murali, S., Thompson, K. P. & Lee, K. S. Gabor-based fusion technique for Optical Coherence Microscopy. *Opt. Express* **18**, 3632–3642 (2010).
- Murali, S., Thompson, K. P. & Rolland, J. P. Three-dimensional adaptive microscopy using embedded liquid lens. *Opt. Lett.* **34**, 145–147 (2009).
- Lee, K. S., Thompson, K. P. & Rolland, J. P. Broadband astigmatism-corrected Czerny–Turner spectrometer. *Opt. Express* **18**, 23378–23384 (2010).



26. Huber, R., Wojtkowski, M. & Fujimoto, J. Fourier Domain Mode Locking (FDML): A new laser operating regime and applications for optical coherence tomography. *Opt. Express* **14**, 3225–3237 (2006).
27. Hsu, K., Meemon, P., Lee, K. S., Delfyett, P. J. & Rolland, J. P. Broadband Fourier-domain mode-locked lasers. *Photonic Sensors* **1**, 222–227 (2011).
28. Lee, K. S., Meemon, P., Dallas, W., Hsu, K. & Rolland, J. P. Dual detection full range frequency domain optical coherence tomography. *Opt. Lett.* **35**, 1058–1060 (2010).
29. Baer, E., Hiltner, P. A. & Shirk, J. S. *Multilayer polymer gradient index* (GRIN) lenses. US patent US7002754 B2 (2006).
30. Moore, D. T. Gradient-index optics: a review. *Appl. Opt.* **19**, 1035–1038 (1980).
31. Fantone, S. D. Optical design with spherical index gradients. *Appl. Opt.* **22**, 1815–1819 (1983).
32. Shirk, J. S., Baer, E. & Hiltner, P. A. Variable refractive index polymer materials. US patent US7255914 B2 (2007).
33. Bouma, B. E. & Tearney, G. J. *Handbook of optical coherence tomography* (Marcel Dekker, Inc., 2002).
34. Lee, K. S., Akcay, A. C., Delemos, T., Clarkson, E. & Rolland, J. P. Dispersion control with a Fourier-domain optical delay line in a fiber-optic imaging interferometer. *Appl. Opt.* **44**, 4009–4022 (2005).
35. Murali, S. et al. Assessment of a liquid lens enabled in vivo optical coherence microscope. *Special Issue on 400 Years of Optical Instrumentation, Editors: Daniel Malacara, Joanna Schmit, Malgorzata Kujawinska, and Mitsuo Takeda, Appl. Opt.* **49**, D145–D156 (2010).
36. Lee, K. S., Thompson, K. P., Meemon, P. & Rolland, J. P. Cellular resolution optical coherence microscopy with high acquisition speed for in-vivo human skin volumetric imaging. *Opt. Lett.* **36**, 2221–2223 (2011).
37. Lee, K. S. et al. Three-dimensional imaging of normal skin and nonmelanoma skin cancer with cellular resolution using Gabor domain optical coherence microscopy. *Journal of biomedical optics* **17**, 126006–126006 (2012).
38. Fercher, A. F., Hitzenberger, C. K., Kamp, G. & El-Zaiat, S. Y. Measurement of intraocular distances by backscattering spectral interferometry. *Opt. Comm.* **117**, 43–48 (1995).
39. Rolland, J. et al. Task-based optimization and performance assessment in optical coherence imaging. *J. Opt. Soc. Am. A* **22**, 1132–1142 (2005).
40. Born, M. & Wolf, E. *Principles of Optics, seventh expanded edition* (Cambridge University Press, 1999).
41. Sorin, W. & Gray, D. Simultaneous thickness and group index measurement using optical low-coherence reflectometry. *IEEE Photonics Technol. Lett.* **4**, 105–107 (1992).
42. Ohmi, M., Ohnishi, Y., Yoden, K. & Haruna, M. In vitro simultaneous measurement of refractive index and thickness of biological tissue by the low coherence interferometry. *IEEE Trans. on Biomed. Eng.* **47**, 1266–1270 (2000).
43. Park, S., Park, K., Kim, Y. & Lee, B. Measurements-Simultaneous Measurements of Refractive Index and Thickness by Spectral-Domain Low Coherence Interferometry Having Dual Sample Probes. *IEEE Photonics Technol. Lett.* **23**, 1076–1078 (2011).
44. Kim, S., Na, J., Kim, M. J. & Lee, B. H. Simultaneous measurement of refractive index and thickness by combining low-coherence interferometry and confocal optics. *Opt. Express* **16**, 5516–5526 (2008).
45. Duma, V. F., Lee, K., Meemon, P. & Rolland, J. P. Experimental investigations of the scanning functions of galvanometer-based scanners with applications in OCT. *Appl. Opt.* **50**, 5735–5749 (2011).

## Acknowledgements

This work was supported by the Manufacturable Gradient Index Optics (M-GRIN) program of the Defense Advanced Research Projects Agency (DARPA) and the NYSTAR Foundation C050070.

## Author contributions

J.P.R. conceived the GD-OCM system and in collaboration with K.P.T. led the design of key custom components. M.P. and E.B. fabricated the S-GRIN components. P.M. and J.P.R. designed the experiments and methods. P.M. and J.Y. conducted the experiments and analyzed the results using the swept-source OCT systems. K.S.L. and J.Y. conducted the experiments and analyzed the results for the GD-OCM system. P.M., J.Y., J.P.R. and K.P.T. wrote the paper with contributions from K.S.L., M.P. and E. B.

## Additional information

**Competing financial interests:** Dr. Ponting is a co-founder and co-owner of PolymerPlus LLC and currently serves as its President. Dr. Ponting has acquired development funding for PolymerPlus through DARPA and the Office of Naval Research in the area of nanolayered polymer materials for use in Gradient Refractive Index (GRIN) optics. Professor Baer is co-founder and co-owner of PolymerPlus LLC. Professor Baer directs research funding for Case Western Reserve University through SAIC/DARPA and the Office of Naval Research in the area of nanolayered polymer systems for use in Gradient Refractive Index (GRIN) optics.

**License:** This work is licensed under a Creative Commons Attribution-NonCommercial-NoDerivs 3.0 Unported License. To view a copy of this license, visit <http://creativecommons.org/licenses/by-nc-nd/3.0/>

**How to cite this article:** Meemon, P. et al. Optical Coherence Tomography Enabling Non Destructive Metrology of Layered Polymeric GRIN Material. *Sci. Rep.* **3**, 1709; DOI:10.1038/srep01709 (2013).